This is a preprint, the final version is subject to change, of the American Mineralogist (MSA)
Cite as Authors (Year) Title. American Mineralogist, in press.
DOI: https://doi.org/10.2138/am-2019-7081

Revision 1

Melting in the Fe-FeO system to 204 GPa: Implications for oxygen in Earth's core

KENTA OKA[1,*], KEI HIROSE[1,2], SHOH TAGAWA[1], YUTO KIDOKORO[1], YOICHI NAKAJIMA[3,*], YASUHIRO KUWAYAMA[1], GUILLAUME MORARD[4], NICOLAS COUDURIER[4], AND GUILLAUME FIQUET[4]

[1]Department of Earth and Planetary Science, The University of Tokyo, 7-3-1 Hongo, Bunkyo, Tokyo 113-0033, Japan

[2]Earth-Life Science Institute, Tokyo Institute of Technology, 2-12-1 Ookayama, Meguro, Tokyo 152-8550, Japan

[3]Department of Physics, Kumamoto University, 2-39-1 Kurokami, Chuo-ku, Kumamoto, Kumamoto 860-8555, Japan

[4]Sorbonne Université, Muséum National d'Histoire Naturelle, UMR CNRS 7590, Institut de Minéralogie, de Physique des Matériaux et de Cosmochimie, IMPMC, 75005 Paris, France

*E-mails: kenta-oka177@g.ecc.u-tokyo.ac.jp (K.O.) and yoichi@kumamoto-u.ac.jp (Y.N.)

ABSTRACT

We performed melting experiments on Fe-O alloys up to 204 GPa and 3500 K in a diamond-anvil cell (DAC) and determined the liquidus phase relations in the Fe-FeO system based on textural and chemical characterizations of recovered samples. Liquid-liquid immiscibility was observed up to 29 GPa. Oxygen concentration in eutectic liquid increased from >8 wt% O at 44 GPa to 13 wt% at 204 GPa, and is extrapolated to be about 15 wt% at the inner core boundary (ICB) conditions. These results support O-rich liquid core, although oxygen cannot be a single

core light element. We estimated the range of possible liquid core compositions in Fe-O-Si-C-S and found that the upper bounds for silicon and carbon concentrations are constrained by the crystallization of dense inner core at the ICB.

INTRODUCTION

Oxygen is one of the likely candidates for light elements in the Earth's core (Hirose et al. 2013; Morard et al. 2017). This hypothesis is supported by recent first-principles calculations showing that both the density and sound velocity observed in the liquid core are compatible with the presence of oxygen (Badro et al. 2014). The earlier calculations by Alfè et al. (2002) also stated that oxygen is an important alloying element in the core; it is mostly partitioned into liquid iron and can thus account for the large density contrast observed across the ICB.

Liquidus phase relations, in particular eutectic composition, provide another clue to constrain the outer core composition. Even if oxygen is likely to be an abundant core light element, the liquid core should not crystallize as FeO at the ICB; FeO is indeed lighter and thus cannot form the denser solid inner core. Previous experiments clearly demonstrated that oxygen concentration in the Fe-FeO eutectic liquid increases with increasing pressure (Ohtani et al. 1984; Ringwood and Hibberson 1990; Seagle et al. 2008). Komabayashi (2014) developed a thermodynamic model that predicts ~12 wt% O in the eutectic liquid composition at 330 GPa corresponding to the pressure at the ICB. The most recent study by Morard et al. (2017) carried out melting experiments on Fe-FeO to 102 GPa. They reported a sharp and large increase in oxygen concentration in the eutectic liquid around 80 GPa, which contradicts earlier experimental results and the thermodynamic model (Seagle et al. 2008; Komabayashi 2014).

Previous experiments showed immiscible Fe-rich metallic liquid and FeO-rich ionic liquid

below 25 GPa (Ringwood and Hibberson 1990; Tsuno et al. 2007). Frost et al. (2010) found a small immiscible two-liquid region at 25 GPa and 2473 K, and the immiscibility is no longer observed at 50 GPa (Seagle et al. 2008). The disappearance of the two-liquid region from the Fe-FeO liquidus diagram should change the eutectic liquid composition as illustrated in Figure 1.

Here we report melting experiments on Fe-O alloys up to pressures of 204 GPa, which extends the pressure range examined in earlier studies by a factor 2. On the basis of the eutectic liquid composition determined in the core pressure range, we discuss the presence of oxygen and other light elements in the outer core.

EXPERIMENTAL METHODS

High-pressure and -temperature (*P*-*T*) conditions were generated in a laser-heated DAC using diamonds with culet size of 120, 150, or 300 μm (Table 1). We employed homogeneous Fe-4.1wt%O and Fe-13.0wt%O starting materials, prepared by magnetron sputtering of Fe in a inductively coupled RF (radio-frequency) reactive oxygen-rich argon plasma (Morard et al. 2017). A sample flake was loaded with an Al_2O_3 pressure medium, into a 40–140 μm hole at the center of a pre-indented rhenium gasket. After loading the sample, the whole DAC was dried in a vacuum oven at 423 K for at least 12 hrs to eliminate moisture from the sample. It was then compressed in an argon atmosphere.

At each pressure of interest, we heated the sample from both sides with a couple of 100 W single-mode Yb fiber lasers (YLR-100, IPG Photonics) with flat-top beam-shaping optics. A visible laser-heated spot was approximately 20 μm in diameter. The heating duration was limited to less than 3 sec, in order to avoid temperature fluctuation that leads to a complex melting texture. It is long enough for oxygen to diffuse over an entire melt pocket (Helffrich 2014) (Figs. 2a, b),

which assures chemical equilibrium between liquid and solid since melting/crystallization occurs almost instantaneously. Indeed, the time-series experiments performed by Mori et al. (2017) demonstrated that the compositions of coexisting liquid and solid in the Fe-S system did not change after 1 sec in a DAC. Note that the diffusivity of oxygen is slightly higher than that of sulfur in liquid Fe (Helffrich 2014). The temperature profile was obtained using a spectro-radiometric method (Mori et al. 2017) (Fig. 2c). Following Mori et al. (2017) and Tateno et al. (2018), we determined the temperature at the liquid/solid boundary by combining the temperature profile with a sample cross section. Pressure was measured at 300 K after heating based on a Raman shift of diamond (anvil) (Akahama and Kawamura 2004) and then corrected for thermal pressure based on Andrault et al. (1998). We considered 60% of theoretical thermal pressure for purely isochoric heating $\Delta P = \alpha K_T \times (T - 300)$, αK_T = 4 MPa/K below 100 GPa, and adopted 90% of that with αK_T = 9 MPa/K for runs at higher pressures (Hirose et al. 2017). These estimates differ from the empirical one (5% pressure increase per temperature increase for every 1000 K) (Fiquet et al. 2010) by less than 7 GPa in all runs. The uncertainties in both *P* and *T* should therefore be less than ±5–10 % (Table 1).

Textural and chemical characterizations were carried out on recovered DAC samples. A cross section of the laser-heated portion of a sample was obtained parallel to the compression axis by milling with a focused Ga ion beam (FIB, *FEI Versa*^{TM} *3D DualBeam*^{TM}). It was then examined by a field-emission (FE)-type scanning electron microscope (SEM) and energy dispersive X-ray spectrometry (EDS) for elemental mapping (Fig. 2a). We also used an FE-type electron probe micro-analyzer (FE-EPMA, JEOL JXA-8530F) with wavelength dispersive spectrometry (WDS) for quantitative chemical analyses; an accelerating voltage of 12 kV, a current of 15 nA, and the X-ray counting time of 20s/10s for peak/background. Fe, Fe_3C, and corundum were used as

standards. LDE1 (O), LIF (Fe), LDE2H (C), and TAP (Al) were analyzing crystals. The FE-EPMA analyses of quenched liquid iron sometimes included a small amount of Al, which is likely a signal from the surrounding pressure medium or Al_2O_3 grains that mechanically intruded into the liquid during the experiment (Figs. 2a, b). Al was therefore subtracted as Al_2O_3 from raw data. Carbon was detected not only in the quenched liquid, but also inside the rhenium gasket; the latter could be due to contamination during FIB processing or FE-EPMA analysis. Thus, we subtracted 0.2–0.4 wt% C from the raw analyses of liquids, which was found on the rhenium gasket in the same cross section (or in an unheated portion of a sample when the gasket was not included). The liquids should have included the remaining 0.8–3.5 wt% C (Table 1).

RESULTS

We performed eight separate runs in a pressure range from 23 to 204 GPa (Table 1). In sample cross sections, except for runs performed below 44 GPa, we found a chemically homogeneous area with non-stoichiometric Fe-O composition at the center of a laser-heated area (Figs. 2a, b), which likely represents a quenched liquid pool. There are layers of single-phase Fe or FeO (or both) next to the liquid, which indicates which side of the eutectic the liquid was. A subsolidus part is found outside such a liquidus phase layer.

In run #1 performed at 23 GPa and 2760 K, two large liquid pools were observed (Fig. 2d); each one exhibits heterogeneous textures, similar to the ones reported in previous multi-anvil experiments (e.g., Ringwood and Hibberson 1990; Tsuno et al. 2007). The two-liquid immiscibility was also found in run #2 at 29 GPa, but not at pressures above 44 GPa in this study.

In runs #3–#6, the composition of a liquid represents the lower and upper bounds for oxygen concentration in the eutectic liquid when coexisting with Fe and FeO, respectively (Table 1, Fig.

117 3). In runs #4 and #6, both Fe and FeO layers were found. As commonly observed in both multi-
118 anvil (e.g., Hirose and Fei 2002) and DAC experiments (e.g., Mori et al. 2017), a temperature
119 gradient in a sample induced phase segregation of each phase; in the present case, the layers of
120 liquid, FeO, and Fe were formed separately. Nevertheless, we estimate the difference in
121 temperature between the liquid/FeO boundary and the FeO/Fe boundary to be less than 50–60 K
122 considering the temperature gradient (Fig. 2c) (note that the FeO layer was about 1 μm wide as
123 shown in Fig. 2a). Since 50–60 K is less than the uncertainty in the present experimental
124 temperature determination, we considered that liquid, FeO, and Fe coexisted practically at the
125 same temperature. The liquid composition may therefore be the eutectic liquid when both Fe and
126 FeO layers were observed. The liquids obtained in runs #7 and #8 included remarkably less oxygen
127 than in the other runs; alternatively, they were enriched in carbon (Table 1). Except for these two
128 runs, the carbon amount was limited to ~1 wt%, with probably a limited effect on the Fe-FeO
129 diagram.

130 The experiments with limited carbon contamination show a change in the Fe-FeO eutectic
131 liquid composition with increasing pressure (Fig. 3). Above 44±4 GPa, the eutectic liquid includes
132 >8 wt% O, which is a remarkably high amount compared to that found in previous multi-anvil
133 experiments below 16 GPa (Ringwood and Hibberson 1990; Tsuno et al. 2007), where liquid-
134 liquid immiscibility is observed. The oxygen concentration increases to about 13 wt% at the
135 maximum pressure of 204±20 GPa explored here.

136 Since the composition of liquid obtained in the present study is close (or identical) to the
137 eutectic liquid composition at each pressure, the liquidus temperature determined as temperature
138 at the liquid/solid boundary should be close to (or represent) the eutectic temperature. Note that
139 the compositions of the present Fe-O-(C) liquids with limited carbon contamination do not

represent the Fe-O-C ternary eutectic compositions. Indeed iron carbides did not crystallize; therefore their liquidus temperatures give the upper bounds for the ternary eutectic temperatures. All data are in good agreement with the Fe-O eutectic melting curve reported by Morard et al. (2017) on the basis of X-ray diffraction (XRD) observations (Fig. 4).

DISCUSSION

The present results show that the eutectic liquid composition in the Fe-FeO binary evolves from Fe + >8 wt% O at 44±4 GPa to +13 wt% O at 204±20 GPa (Fig. 3). This observation is in reasonable agreement with the previous DAC experiments by Seagle et al. (2008) based on the disappearance of Fe or FeO from the XRD pattern, and with the thermodynamic model proposed by Komabayashi (2014) considering a non-ideal mixing based on Frost et al. (2010). Extrapolation of our data to 330 GPa suggests that the Fe-FeO eutectic liquid contains about 15 wt% O at the ICB.

We observed the liquid immiscibility to 29±3 GPa and 2900±290 K, while Frost et al. (2010) found a narrow Fe-FeO immiscible two-liquids region at 25 GPa and 2473 K. These two conditions are similar when considering errors in P and T for both the experiments. In addition, since the textures of quenched immiscible liquids are quite heterogeneous (see Fig. 9 in Frost et al. 2010 and Fig. 2d in this study), a precise determination of their chemical compositions is difficult. Indeed, the compositions of the immiscible two liquids reported by Frost and others include large uncertainties, suggesting that the immiscible two-liquids region may exist to P-T conditions higher than 25 GPa at 2473 K to a certain extent.

The vanishing of the liquid immiscibility changes the Fe-FeO liquidus curves. According to previous experiments (Ohtani et al. 1984; Ringwood and Hibberson 1990), the Fe-FeO eutectic

liquid includes minor amounts of oxygen at low pressures (~2 wt% at 16 GPa). The immiscible two-liquids region is found around Fe+11wt%O to >25 GPa at 2473 K according to Frost et al. (2010). Using the Fe-13.0wt%O starting material, we observed two immiscible liquids at 23 and 29 GPa (Fig. 2c). A single liquid was formed at 44 GPa, suggesting the disappearance of the immiscible two-liquids region from the phase diagram. As illustrated in Fig. 1, a reduction in the immiscible two-liquids region with increasing pressure causes the Fe-FeO eutectic point to shift to a more O-rich region. It explains the high (>8 wt%) oxygen concentration in the eutectic liquid at 44±4 GPa (Fig. 3).

The closure of immiscible two-liquids region also indicates that mixing between liquids Fe and FeO is non-ideal at low pressures and becomes closer to ideal above 44 GPa. It is supported by the eutectic melting curve shown in Fig. 4 that is in broad agreement with the thermodynamic prediction by Komabayashi (2014) considering the ideal mixing. Furthermore, the pressure–eutectic liquid composition relation observed in the present experiments is consistent with the behavior shown by the non-ideal mixing model below ~50 GPa, while it could be explained by the ideal solution model at higher pressures (Komabayashi 2014) (Fig. 3). The ideal solution model by Komabayashi shows the lower oxygen concentration in the Fe-FeO eutectic liquid than the present experimental results at >50 GPa, but his thermodynamic prediction depends on the uncertain melting temperature of FeO, which can be much lower than he assumed.

While these results suggest that the oxygen content in the eutectic liquid increases with increasing pressure to ~40 GPa, Morard et al. (2017) demonstrated it rises sharply around 80 GPa (Fig. 3). The liquid coexisting with both Fe and FeO at 39 GPa in run #7 was contaminated by 3.1 wt% C and included only 0.4 wt% O, much less than that in the Fe-FeO eutectic liquid at equivalent pressure. It is possible that the incorporation of carbon expands the immiscible two-liquid region

to higher pressures, which could explain the difference between these two studies. Morard et al. (2017) estimated 0.8–2.7 wt% C with ±1.0 wt% uncertainty for liquids obtained below 80 GPa, using Rietveld analyses of XRD patterns to find the amount of iron carbide formed in a quenched liquid portion (after moderate re-heating after melting experiments). Since solid Fe can include 1 to 2 wt% C below 100 GPa (Walker et al. 2013; Fei and Brosh 2014), such estimates may be underestimated. The observed low O content may be more relevant to the ternary Fe-O-C system than for the binary Fe-FeO system.

IMPLICATIONS

In order to form the dense inner core, the liquid core should crystallize Fe that is depleted in light elements compared to the outer core liquid. It was once suggested that the inner core is composed mainly of Fe_7C_3 (Chen et al. 2014; Prescher et al. 2015), but recent calculations demonstrated that the density of Fe_7C_3 is too small for the inner core (Li et al. 2016). The present experiments demonstrate that oxygen concentration in the Fe-FeO eutectic liquid increases (in other words, the liquidus field of Fe expands) with increasing pressure (Fig. 3). It contrasts the other binary iron alloy systems. The amounts of silicon, carbon, and sulfur in corresponding Fe-Si (Ozawa et al. 2016), Fe-C (Lord et al. 2009; Mashino et al. 2019), and Fe-S binary eutectic liquids (Kamada et al. 2012; Mori et al. 2017) decrease at higher pressures. At 330 GPa, these amounts are less than those required to explain the outer core density deficit when assuming a single light element. It indicates that none of silicon, carbon, and sulfur can be a predominant light component in the core.

The present experiments allow us to determine the Fe-FeO eutectic liquid composition to 204 GPa, which is a much higher pressure compared to earlier experiments (Seagle et al. 2008; Morard

et al. 2017). Our extrapolation to 330 GPa indicates ~15 wt% O in the eutectic liquid at the ICB conditions. If oxygen is assumed to be the sole light element in the core, the calculations by Badro et al. (2014) argued that 5.4 wt% O is required to account for both the density and bulk sound velocity in the outer core. If this amount (Fe + 5.4 wt% O) is retained, such a system should sit on the Fe-rich side of the eutectic and thus crystallize solid Fe at the ICB, which is consistent with a dense inner core. However, oxygen is hardly soluble in solid Fe (<0.1 wt% at ICB conditions - see Alfè et al. 2002; Ozawa et al. 2010). And the inner core is less dense than pure iron to some extent (Antonangeli and Ohtani, 2015), thus suggesting that oxygen cannot be the sole light element in the core.

Even if oxygen is not a predominant light element, the core should include (or should have included) a certain amount of oxygen (Hirose et al. 2017), according to recent high-temperature core formation models (e.g., Siebert et al. 2013). The present estimate of the Fe-FeO eutectic liquid composition at 330 GPa is thus important for modeling the compositional evolution of the Earth's core and for constraining the present-day core composition from the phase diagrams of iron alloys. Recently Tateno et al. (2018) examined the liquidus phase relations in the Fe-Si-S ternary system and found that the liquidus field of solid Fe is approximated by a tie-line connecting the two eutectic points in the Fe-Si and Fe-S binary systems. If this is also true in Fe alloy systems containing more light elements, we can estimate the liquidus field of solid Fe in Fe-O-Si-C-S at the ICB, considering each binary eutectic liquid composition that has been already reported in the literature: 15 wt% O in Fe-O (this study), 1.5 wt% Si in Fe-Si (Ozawa et al. 2016), 3 wt% C in Fe-C (Mashino et al. 2019), and 5 wt% S in Fe-S (Mori et al. 2017).

The present-day outer core composition should be within the liquidus field of solid Fe at 330 GPa. It provides an additional constraint to narrow down the possible range for the outer core

232 composition (Fig. 5). The first-principles calculations by Badro et al. (2014) showed the range of
233 liquid Fe-O-Si-C-S compositions that explain both the density and sound velocity of the outer core.
234 That range is reduced when we consider such additional conditions required to form a dense inner
235 core. While Badro and others suggested that the silicon content could be as high as 4.5 wt%, the
236 amount of silicon in the possible liquid core composition is found to be small, and constrained by
237 the Fe-Si eutectic liquid composition. The estimate of sulfur concentration is similar. The minor
238 silicon content in the present-day outer core is consistent with the limited Si+O solubility in molten
239 iron under the core *P-T* conditions (Hirose et al. 2017). In addition, Badro et al. (2014)
240 demonstrated that the carbon content can be as high as 3.9 wt%, but our new constraint limits it to
241 less than 2.5 wt%.
242

243 **ACKNOWLEDGMENTS**

244 We thank K. Yonemitsu for help in sample analyses with FIB, EDS, and EPMA. Comments
245 from three anonymous reviewers helped improve this paper substantially. This work was supported
246 by the JSPS grant no. 16H06285 to K.H. G.M., N.C., and G.F. acknowledge funding from the
247 European Research Council (ERC) under the European Union's Horizon 2020 Research and
248 Innovation program (ERC Planet Dive, grant agreement N° 670787).
249

250 **REFERENCES CITED**

251 Akahama, Y., and Kawamura, H. (2004) High-pressure Raman spectroscopy of diamond anvils to
252 250GPa: Method for pressure determination in the multimegabar pressure range. Journal of
253 Applied Physics, 96, 3748–3751.
254 Alfè, D., Gillan, M.J., and Price, G.D. (2002) Composition and temperature of the Earth's core

constrained by combining ab initio calculations and seismic data. Earth and Planetary Science Letters, 195, 91–98.

Andrault, D., Fiquet, G., Itié, J.-P., Richet, P., Gillet, P., Häusermann, D., and Hanfland, M. (1998) Thermal pressure in the laser-heated diamond-anvil cell: An X-ray diffraction study. European Journal of Mineralogy, 10, 931–940.

Antonangeli, D., and Ohtani, E. (2015) Sound velocity of hcp-Fe at high pressure: Experimental constraints, extrapolations and comparison with seismic models. Progress in Earth and Planetary Science, 2:3.

Badro, J., Côte, A.S., and Brodholt, J.P. (2014) A seismologically consistent compositional model of Earth's core. Proceedings of the National Academy of Sciences USA, 111, 7542–7545.

Chen, B., Li, Z., Zhang, D., Liu, J., Hu, M.Y., Zhao, J., Bi, W., Alp, E.E., Xiao, Y., Chow, P., and others (2014) Hidden carbon in Earth's inner core revealed by shear softening in dense Fe_7C_3. Proceedings of the National Academy of Sciences, 111, 17755–17758.

Fei, Y., and Brosh, E. (2014) Experimental study and thermodynamic calculations of phase relations in the Fe–C system at high pressure. Earth and Planetary Science Letters, 408, 155–162.

Fiquet, G., Auzende, A.L., Siebert, J., Corgne, A., Bureau, H., Ozawa, H., and Garbarino, G. (2010) Melting of Peridotite to 140 Gigapascals. Science, 329, 1516–1518.

Frost, D.J., Asahara, Y., Rubie, D.C., Miyajima, N., Dubrovinsky, L.S., Holzapfel, C., Ohtani, E., Miyahara, M., and Sakai, T. (2010) Partitioning of oxygen between the Earth's mantle and core. Journal of Geophysical Research, 115, B02202.

Helffrich, G. (2014) Outer core compositional layering and constraints on core liquid transport properties. Earth and Planetary Science Letters, 391, 256–262.

278 Hirose, K., and Fei, Y. (2002) Subsolidus and melting phase relations of basaltic composition in
279 the uppermostlower mantle. Geochimica et Cosmochimica Acta, 66, 2099–2108.
280 Hirose, K., Labrosse, S., and Hernlund, J. (2013) Composition and state of the core. Annual
281 Review of Earth and Planetary Sciences, 41, 657–691.
282 Hirose, K., Morard, G., Sinmyo, R., Umemoto, K., Hernlund, J., Helffrich, G., and Labrosse, S.
283 (2017) Crystallization of silicon dioxide and compositional evolution of the Earth's core.
284 Nature, 543, 99–102.
285 Kamada, S., Ohtani, E., Terasaki, H., Sakai, T., Miyahara, M., Ohishi, Y., and Hirao, N. (2012)
286 Melting relationships in the Fe–Fe_3S system up to the outer core conditions. Earth and
287 Planetary Science Letters, 359/360, 26–33.
288 Komabayashi, T. (2014) Thermodynamics of melting relations in the system Fe-FeO at high
289 pressure: Implications for oxygen in the Earth's core. Journal of Geophysical Research: Solid
290 Earth, 119, 4164–4177.
291 Li, Y., Vočadlo, L., Brodholt, J., and Wood, I.G. (2016) Thermoelasticity of Fe_7C_3 under inner
292 core conditions. Journal of Geophysical Research: Solid Earth, 121, 5828–5837.
293 Lord, O.T., Walter, M.J., Dasgupta, R., Walker, D., and Clark, S.M. (2009) Melting in the Fe-C
294 system to 70 GPa. Earth and Planetary Science Letters, 284, 157–167.
295 Mashino, I., Miozzi, F., Hirose, K., Morard, G., and Sinmyo, R. (2019) Melting experiments on
296 the Fe–C binary system up to 255 GPa: Constraints on the carbon content in the Earth's core.
297 Earth and Planetary Science Letters, 515, 135–144.
298 Morard, G., Andrault, D., Antonangeli, D., Nakajima, Y., Auzende, A.L., Boulard, E., Cervera, S.,
299 Clark, A., Lord, O.T., Siebert, J., and others (2017) Fe–FeO and Fe–Fe_3C melting relations
300 at Earth's core–mantle boundary conditions: Implications for a volatile-rich or oxygen-rich

core. Earth and Planetary Science Letters, 473, 94–103.

Mori, Y., Ozawa, H., Hirose, K., Sinmyo, R., Tateno, S., Morard, G., and Ohishi, Y. (2017) Melting experiments on Fe–Fe_3S system to 254 GPa. Earth and Planetary Science Letters, 464, 135–141.

Ohtani, E., Ringwood, A.E., and Hibberson, W. (1984) Composition of the core II. Effect of high pressure on solubility of FeO in molten iron, Earth and Planetary Science Letters, 71, 94–103.

Ozawa, H., Hirose, K., Tateno, S., Sata, N., and Ohishi, Y. (2010) Phase transition boundary between B1 and B8 structures of FeO up to 210 GPa. Physics of the Earth and Planetary Interiors, 179, 157–163.

Ozawa, H., Hirose, K., Yonemitsu, K., and Ohishi, Y. (2016) High-pressure melting experiments on Fe–Si alloys and implications for silicon as a light element in the core. Earth and Planetary Science Letters, 456, 47–54.

Prescher, C., Dubrovinsky, L., Bykova, E., Kupenko, I., Glazyrin, K., Kantor, A., McCammon, C., Mookherjee, M., Nakajima, Y., Miyajima, N., and others (2015) High Poisson's ratio of Earth's inner core explained by carbon alloying. Nature Geoscience, 8, 220–223.

Ringwood, A.E., and Hibberson, W. (1990) The system Fe-FeO revisited. Physics and Chemistry of Minerals, 17, 313–319.

Seagle, C.T., Heinz, D.L., Campbell, A.J., Prakapenka, V.B., and Wanless, S.T. (2008) Melting and thermal expansion in the Fe-FeO system at high pressure. Earth and Planetary Science Letters, 265, 655–665.

Siebert, J., Badro, J., Antonangeli, D., and Ryerson, F.J. (2013) Terrestrial accretion under oxidizing conditions. Science, 339, 1194–1197.

Tanaka, T., and Nagasaka, T. (2006) Fundamentals of thermodynamics of phase diagrams. Ferrum,

11, 15–22 (in Japanese).

Tateno, S., Hirose, K., Sinmyo, R., Morard, G., Hirao, N., and Ohishi, Y. (2018) Melting experiments on Fe–Si–S alloys to core pressures: Silicon in the core? American Mineralogist, 103, 742–748.

Tsuno, K., Ohtani, E., and Terasaki, H. (2007) Immiscible two-liquid regions in the Fe-O-S system at high pressure: Implications for planetary cores. Physics of the Earth and Planetary Interiors, 160, 75–85.

Walker, D., Dasgupta, R., Li, J., Buono, A. (2013) Nonstoichiometry and growth of some Fe carbides. Contributions to Mineralogy and Petrology, 166, 935–957.

Figure captions

FIGURE 1. Schematic illustration of the change in liquidus curve and eutectic point with changing interaction energy in liquid after Tanaka and Nagasaka (2006).

FIGURE 2. Sample cross sections and temperature profile. **(a)** X-ray maps combining oxygen (red) and aluminum (cyan) for a sample recovered from run #6 performed at 204 GPa and 3500 K. Back-scattered electron image shows the liquid/solid boundary. **(b, c)** SEM image and the corresponding temperature profile for run #5 at 132 GPa. The boundary between quenched liquid and solid Fe is found on the basis of the difference in microtexture and the presence of Al_2O_3 grains (black) that mechanically intruded from surroundings into a liquid. The temperature at the liquid-solid boundary is estimated to be 3050 K, considering that the boundary was isothermal (the same temperature for both sides). **(d)** The SEM image from run #1 showing immiscible two liquids at 23 GPa.

FIGURE 3. Oxygen concentration in liquid (red symbols). Normal and reverse triangles indicate liquids coexisting with either one of solid Fe or FeO, respectively, giving the lower and upper bounds for eutectic liquid composition. Diamonds show liquids coexisting with both Fe and FeO that may represent the eutectic liquids. Closed circles are carbon-contaminated samples (>3 wt% C). Black diamonds represent eutectic compositions at 3 GPa (Ohtani et al. 1984) and 16 GPa (Ringwood and Hibberson 1990). Red, blue, and black curves show the change in the Fe-FeO eutectic liquid composition from this study (only with ~1 wt% carbon contamination), Morard et al. (2017), and Seagle et al. (2008), respectively. Green and cyan curves are the thermodynamic models assuming non-ideal and ideal solutions, respectively, by Komabayashi (2014).

FIGURE 4. Fe-FeO eutectic melting curve. Diamonds represent eutectic temperature obtained at 3 GPa (Ohtani et al. 1984), 16 GPa (Ringwood and Hibberson 1990), and 48 and 204 GPa (this study). Reverse triangles indicate the upper bounds for the eutectic temperature. Red and black lines are the Fe-FeO eutectic melting curves obtained in this study and by Morard et al. (2017), respectively. Small circles and squares are the previous experimental data by Seagle et al. (2008) and Morard et al. (2017), respectively, showing the upper (filled) and lower bounds (open symbols) for eutectic temperatures.

FIGURE 5. The range of possible Fe-O-Si-C-S liquid core compositions that crystallize solid Fe at the ICB and account for the density and velocity of the outer core (Badro et al. 2014).

This is a preprint, the final version is subject to change, of the American Mineralogist (MSA)
Cite as Authors (Year) Title. American Mineralogist, in press.
DOI: https://doi.org/10.2138/am-2019-7081

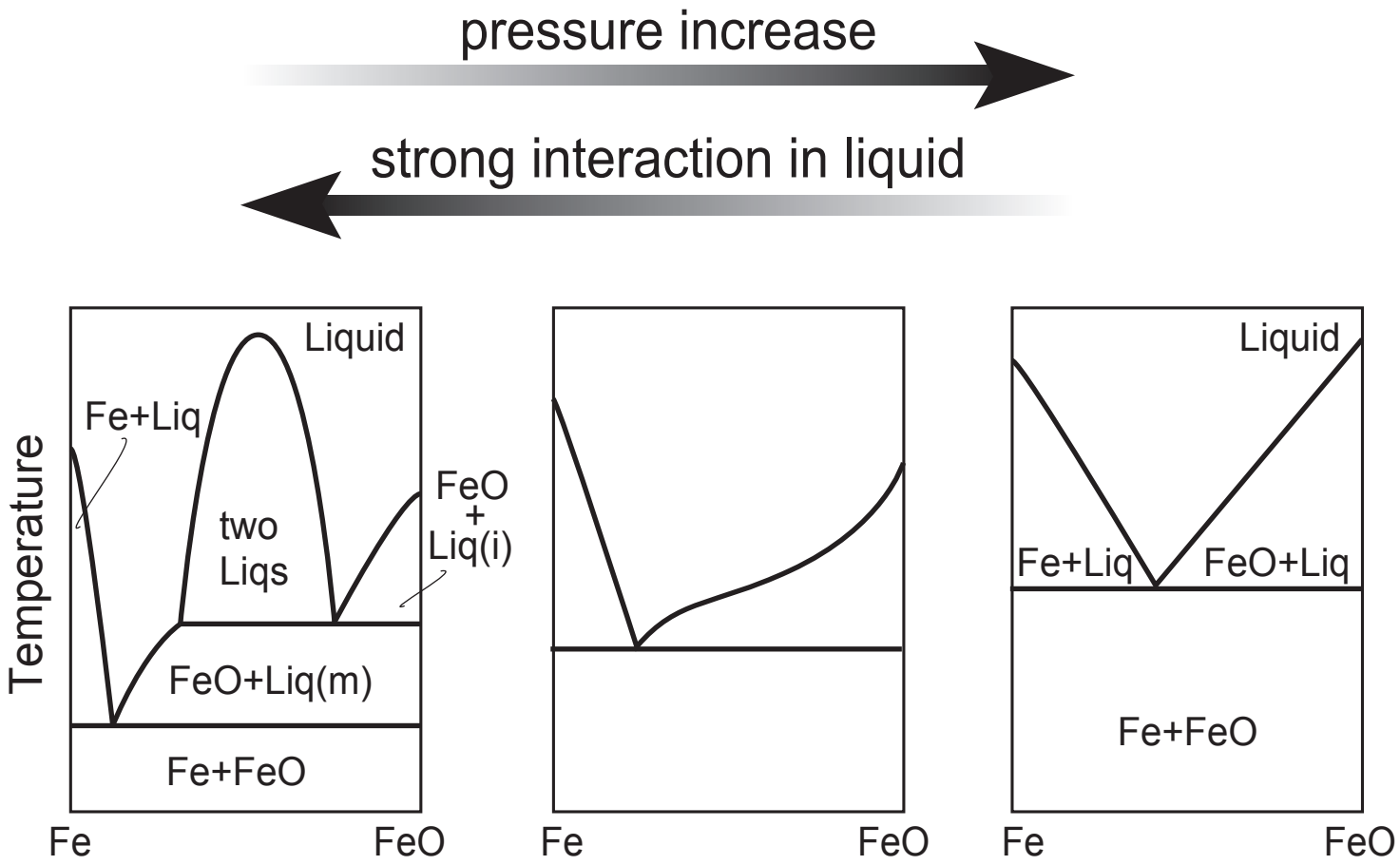

Fig. 1

This is a preprint, the final version is subject to change, of the American Mineralogist (MSA)
Cite as Authors (Year) Title. American Mineralogist, in press.
DOI: https://doi.org/10.2138/am-2019-7081

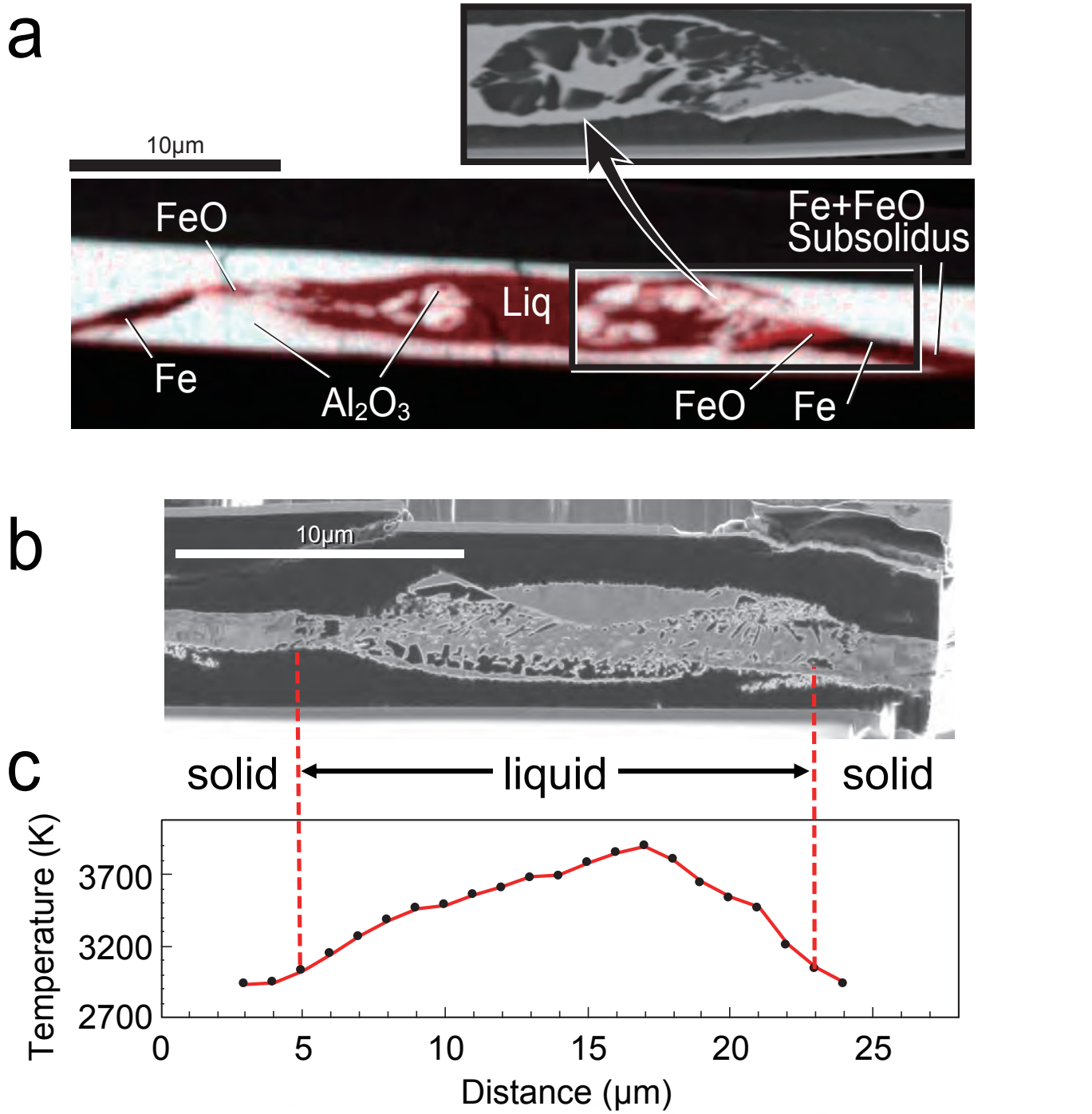

Fig. 2

This is a preprint, the final version is subject to change, of the American Mineralogist (MSA)
Cite as Authors (Year) Title. American Mineralogist, in press.
DOI: https://doi.org/10.2138/am-2019-7081

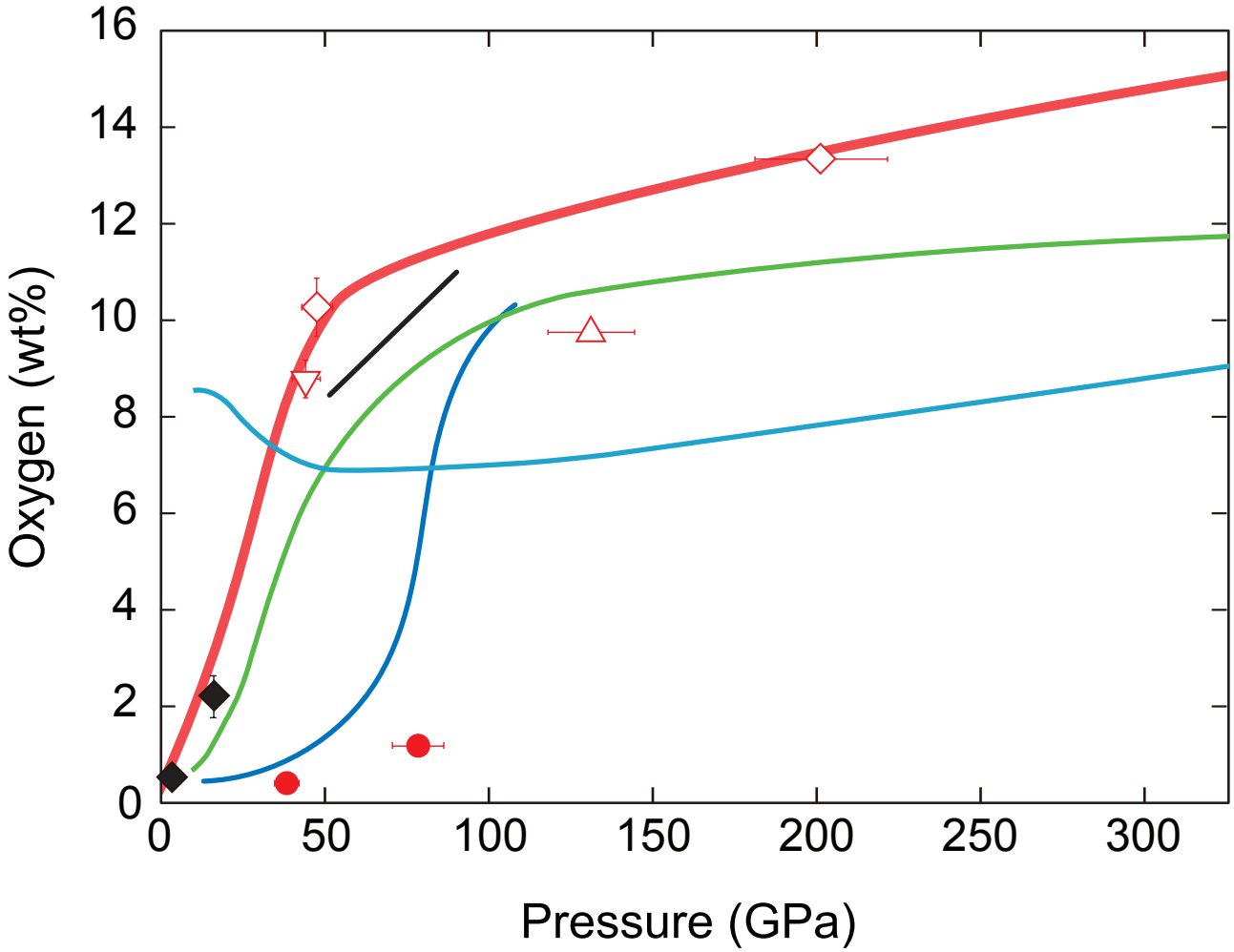

Fig. 2

This is a preprint, the final version is subject to change, of the American Mineralogist (MSA)
Cite as Authors (Year) Title. American Mineralogist, in press.
DOI: https://doi.org/10.2138/am-2019-7081

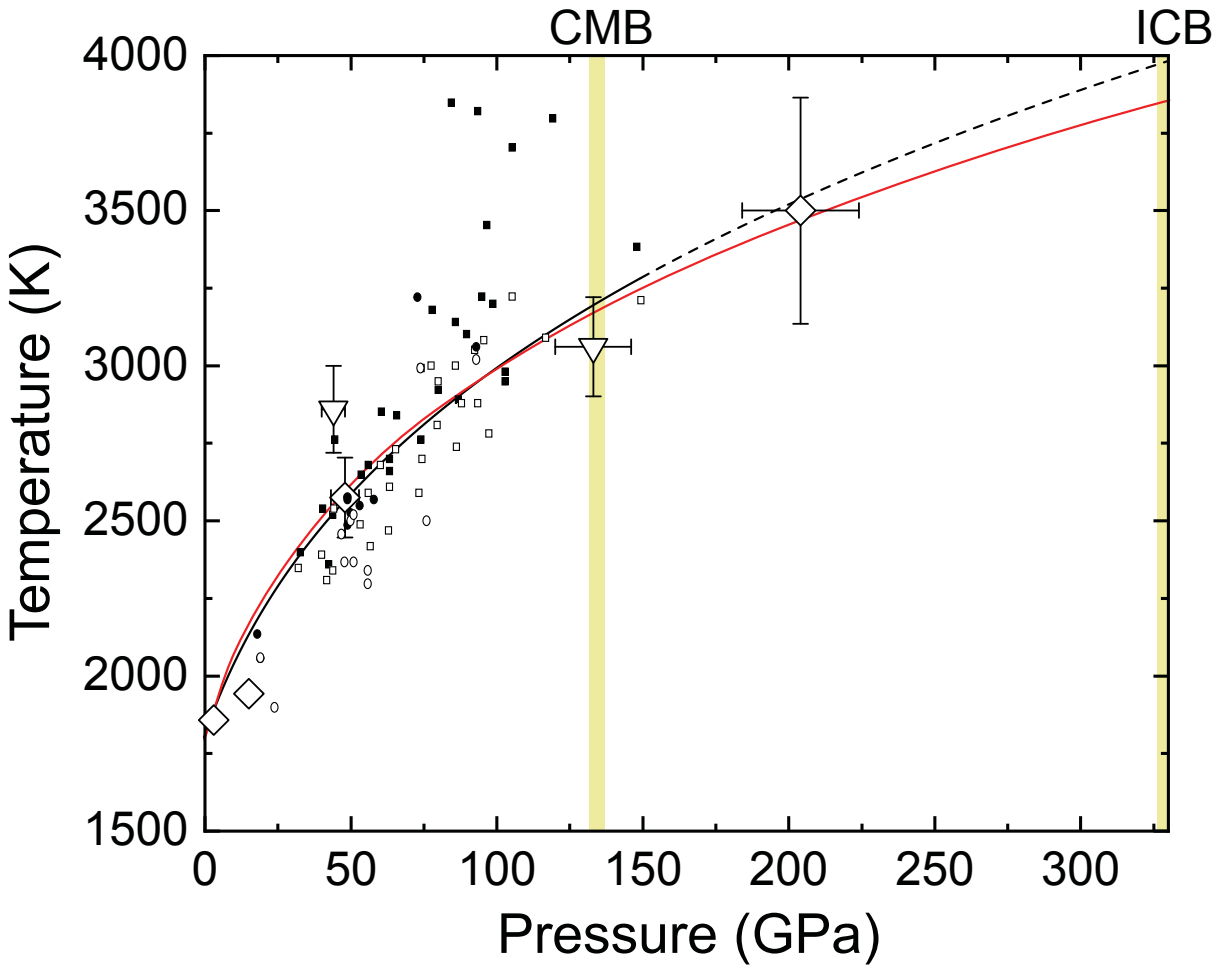

Fig. 4

This is a preprint, the final version is subject to change, of the American Mineralogist (MSA)
Cite as Authors (Year) Title. American Mineralogist, in press.
DOI: https://doi.org/10.2138/am-2019-7081

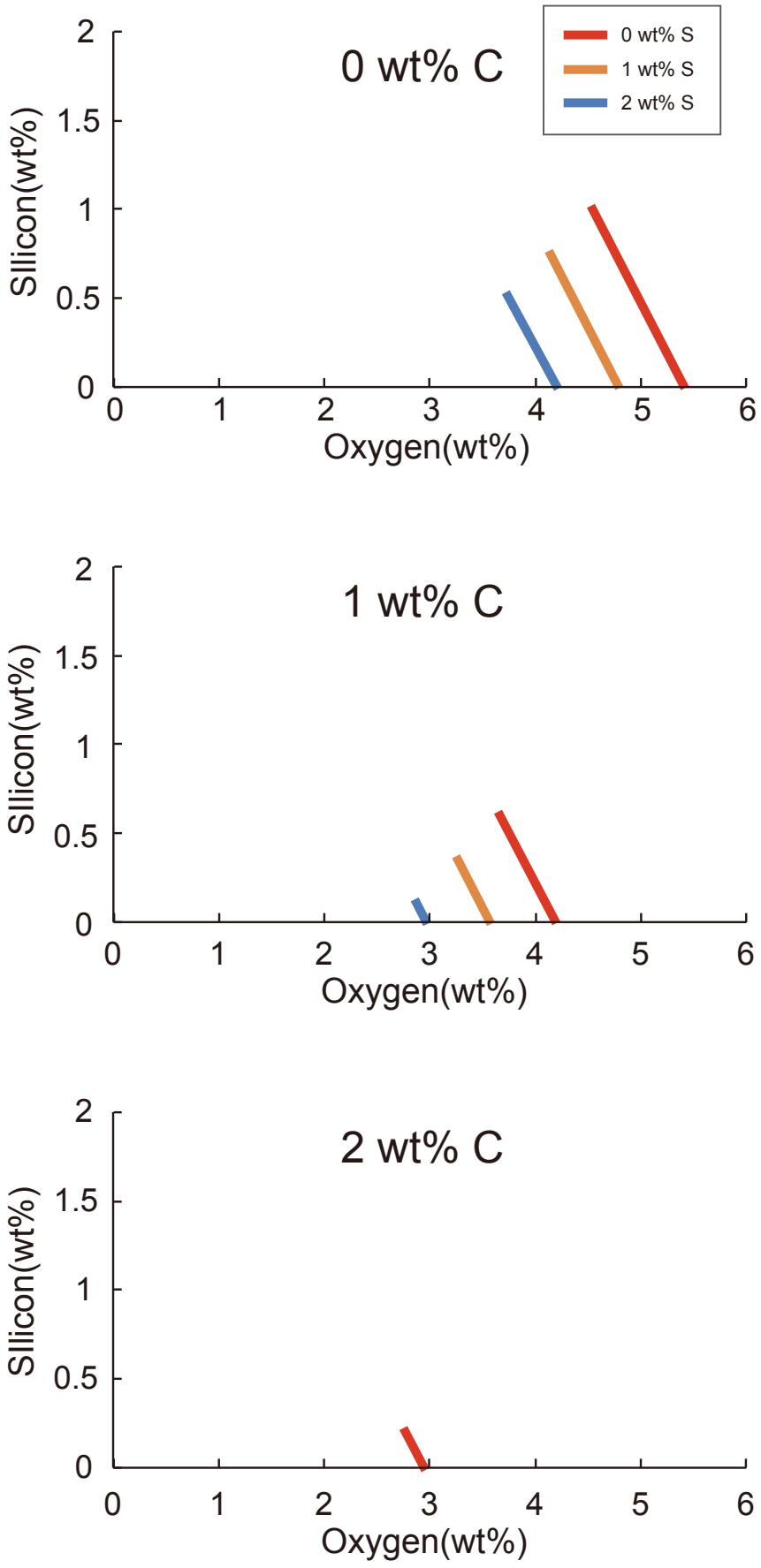

Fig. 5

This is a preprint, the final version is subject to change, of the American Mineralogist (MSA)
Cite as Authors (Year) Title. American Mineralogist, in press.
DOI: https://doi.org/10.2138/am-2019-7081

TABLE 1. Experimental conditions and results

Run #	Starting material	*P* (GPa) at 300 K	*P* (GPa)	*T* (K)	O (wt%) in liquid	C (wt%) in liquid	Coexisting solid phase
#1	Fe-13.0wt%O	17	23(2)	2760(280)	two liquids		none
#2	Fe-13.0wt%O	23	29(3)	2900(290)	two liquids		FeO
#3	Fe-13.0wt%O	38	44(4)	2860(140)	8.8(4)	1.3(1)	FeO
#4	Fe-13.0wt%O	43	48(5)	2580(130)	10.3(6)	1.4(1)	Fe + FeO
#5	Fe-4.1wt%O	110	132(13)	3050(150)	9.8(1)	0.8(0)	Fe
#6	Fe-13.0wt%O	178	204(20)	3500(350)	13.3(0)	1.1(0)	Fe + FeO
#7	Fe-4.1wt%O	34	39(4)	2260(110)	0.4(0)	3.1(1)	Fe + FeO
#8	Fe-4.1wt%O	74	79(8)	2310(120)	1.0(0)	3.5(1)	FeO